Mechanical & Materials Engineering Faculty Publications

Mechanical & Materials Engineering, Department of

2016

An organosilane self-assembled monolayer incorporated into polymer solar cells enabling interfacial coherence to improve charge transport

Zhiqi Li
Jilin University

Xinyuan Zhang
Jilin University

Zhihui Zhang
Jilin University

Shujun Li
Jilin University

Chunyu Liu
Jilin University

See next page for additional authors

Authors

Zhiqi Li, Xinyuan Zhang, Zhihui Zhang, Shujun Li, Chunyu Liu, Liang Shen, Wenbin Guo, and Shengping Ruan

An organosilane self-assembled monolayer incorporated into polymer solar cells enabling interfacial coherence to improve charge transport

Zhiqi Li,[a] Xinyuan Zhang,[a] Zhihui Zhang,[a] Shujun Li,[a] Chunyu Liu,[a] Liang Shen,[ab] Wenbin Guo*[a] and Shengping Ruan*[a]

The reproducible silylation of titanium oxide (TiO_2) with small molecular (dichloromethyl) dimethyl-chlorosilane (DCS) as the cathode buffer layer was developed to improve electron extraction. Through incorporating the DCS capping layer into polymer solar cells (PSCs), the interfacial coherence of devices could be enhanced, leading to a shift in nanocrystallite size and a smaller internal charge transport resistance. Furthermore, a TiO_2/DCS combined interfacial layer could serve as both an exciton dissociation center and a charge transfer channel, which results in a reduction in the energy barrier and electron loss, improving hole-blocking and surface-state passivation in the TiO_2 interfacial layer. The Kelvin probe measurements demonstrate that the employment of the DCS nanolayer decreases conduction band energy of TiO_2 *via* forming a dipole layer at the interface of TiO_2 and the DCS nanolayer, which tunes the work-function of the device and ulteriorly enhances charge carrier transfer between the electrode and the active layer. As a result, the photocurrent and the fill factor of the PSCs are both increased, resulting in an increased power conversion efficiency (PCE) of 6.959%.

1. Introduction

Inverted polymer solar cells (PSCs) consisting of a cathodic indium-tin-oxide (ITO) substrate and a high work-function metal as the top anode have been extensively investigated in recent years.[1–6] Although the employment of air-stable top electrodes such as silver (Ag), aluminum (Al), and gold (Au) in an inverted structure has achieved better air stability by self-encapsulating and avoiding the corrosion by hygroscopic poly(3,4-ethylenedioxylenethiophene):poly(styrenesulphonic acid) (PEDOT:PSS),[7–11] poor electron transfer and high carrier recombination continue to be critical problems for realizing commercial applications of PSCs.[12] To improve charge carrier collection and decrease transporting recombination between the active layer and electrodes, transition metal oxides such as TiO_2, ZnO, WO_3, and MoO_3 are usually used as charge transfer or blocking layers.[13–15] Though the typical inverted PSCs show an ohmic contact for hole injection, intrinsic limitations of sol–gel based metal oxides and the inherent incompatibility of

the electron buffer layer result in a large energy barrier between the inorganic metal oxide and the organic active layer, leading to an unbalanced electron transfer and inefficient electron–hole recombination, and thus the low fill factor (FF) and current density (J_{sc}) cause a decreased power conversion efficient (PCE).[16–19] Therefore, enhancing electron transport and injection at the cathode and reducing the inherent incompatibility at the organic active layer/inorganic metal oxide interface are essential for decreasing the contact resistance and boosting the device efficiency. An excellent electron transport layer capping on the transparent conductive electrode requires high electron mobility, high transparency, and appropriate energy alignment with the lowest unoccupied molecular orbital (LUMO) of the acceptor.[20–22] Hence, higher device efficiency can be obtained by taking advantage of an excellent electron transport layer. A few kinds of materials have been employed to improve electron extraction capacity *via* modifying the interfacial layer of inverted PSCs, including cesium carbonate (CS_2CO_3), cesium fluoride (CSF), titanium chelate (TIPD, TOPD), quantum dots (QDs), and self-assembled dipole molecules (SAM).[23–29] Among them, the interface modification using self-assembled dipole molecules was proved to be a simple and effective way to enhance the electron selectivity of the PSCs because of the capability of controlling the upper layer growth mode and distribution of phases, passivating inorganic surface trap states, and shifting the interfacial energy offset between electrode materials.[30–32]

[a] *State Key Laboratory on Integrated Optoelectronics, Jilin University, College of Electronic Science and Engineering, 2699 Qianjin Street, Changchun 130012, People's Republic of China. E-mail: guowb@jlu.edu.cn, ruansp@jlu.edu.cn*

[b] *Department of Mechanical and Materials Engineering and Nebraska Center for Materials and Nanoscience, University of Nebraska–Lincoln, Lincoln, Nebraska 68588-0656, USA*

This journal is © the Owner Societies 2016

Phys. Chem. Chem. Phys., 2016, **18**, 16005–16012 | **16005**

In this contribution, the self-assembled nanolayer of small molecular (dichloromethyl)dimethylchlorosilane (DCS) was used to modify the cathode buffer layer of PSCs.[33] The incorporation of the TiO$_2$/DCS electron transport layer improved the energy level matching between the ITO and HOMO levels of the active layer and optimized the electrical contact between the hydrophobic organic layer and the hydrophilic metal oxide. Furthermore, the DCS layer lowered the conduction band energy of the TiO$_2$ layer *via* the formation of an interfacial dipole layer at the interfaces of the TiO$_2$ film and ulteriorly decreased the energy barrier between the electrode and the active layer, leading to an enhanced electron transfer ability and surface-state passivation in the buffer layer. As a result, J_{sc} and FF of PSCs are both increased, which leads to an increased PCE of 6.959%. This study demonstrates that a DCS SAM can act as an efficient molecular modification layer on polymer photovoltaic devices.

2. Experimental section

PSCs were fabricated on the commercial indium tin oxide (ITO)-coated glass substrate with the structure of ITO/TiO$_2$/DCS/PCDTBT:PC$_{71}$BM/MoO$_3$/Ag. Firstly, the ITO coated glass substrate was cleaned with acetone, alcohol, and deionized water, respectively, and subsequently dried with nitrogen. Anatase TiO$_2$ was spin-cast from aqueous solution to form a film of 40 nm. In order to optimise the density of surface hydroxyl groups, the TiO$_2$ substrates were subjected to the ethylene glycol (EG) solution of potassium hydroxide (KOH) for 10 min and then transferred to a drying oven. Afterwards, the self-assembly reaction was performed in an atmosphere of dried air by using different concentrations of DCS on the surface of TiO$_2$. The corresponding devices with the DCS thickness of 1, 3, 6, 9, and 12 nm were labeled Device B, Device C, Device D, Device E, and Device F, and the control device without the DCS layer was named as Device A. Then, a solution containing a mixture of PCDTBT:PC$_{71}$BM (7 mg mL^{-1} : 28 mg mL^{-1} by weight) in 1-2-dichlorobenzene solvent was spin-cast on top of the TiO$_2$ layer. The film was dried for 20 min at 70 °C in the glove box. Finally, a MoO$_3$ (4 nm) and an Ag (100 nm) electrode were deposited by thermal evaporation in a vacuum of about 1×10^{-5} Torr in turn. Current density–voltage (J–V) characteristics of the devices were measured using a Keithley 236 Source Measure Unit under an Air Mass 1.5 Global (AM 1.5 G) solar simulator with an irradiation intensity of 100 mW cm^{-2}.[34]

3. Results and discussion

3.1 Morphology analysis

The device layout and the chemical structure of DCS used in this paper are shown in Fig. 1. DCS possesses the conjugated small molecule chlorosilane core and the –Cl (electron-withdrawing) terminal group. The head groups of the DCS have a high affinity surface with –OH groups, which facilitates the spontaneous self-assembly of the molecules onto the hydrophilic surfaces of the
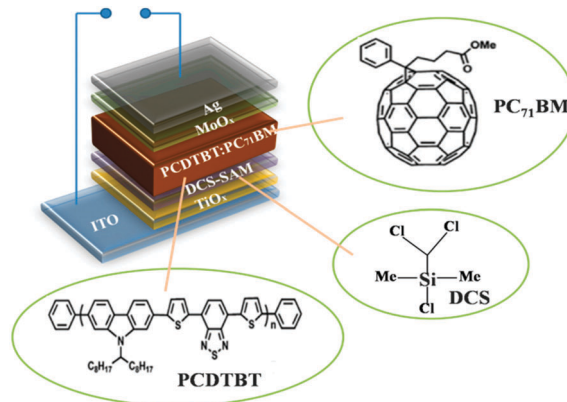

Fig. 1 The scheme diagram of polymer solar cells and molecular structures of PCDTBT, PC$_{71}$BM, and DCS.
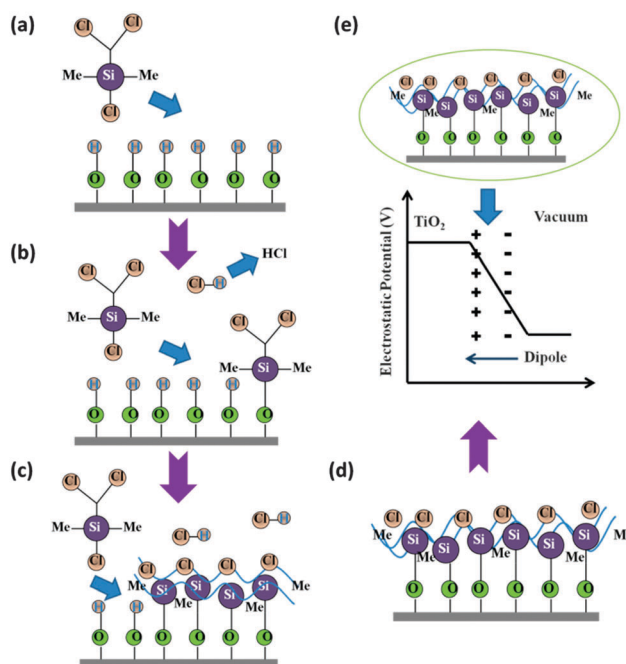

Fig. 2 The detailed self-assembly process of DCS on the TiO$_2$ surface: (a) the hydrophilic surfaces of the TiO$_2$ film, (b) the head groups of the DCS attracted with –OH groups, (c) the electrostatic self-assembly of DCS, (d) the electrostatic self-assembly of DCS leads to the immediate and uniform formation of the interface between the DCS and TiO$_2$ layers, (e) electrostatic potential of TiO$_2$/DCS layer.

TiO$_2$ film. When DCS is deposited on the hydroxylated surface of TiO$_2$ from its aqueous solution, the electrostatic self-assembly of DCS occurs,[35] which is presented in Fig. 2(a)–(d). The positively charged amines (protonated amines) of DCS strongly interact with the negatively charged terminal oxygen ions of the TiO$_2$ surface and then spontaneously alter the conformation of the polymer chains. The electrostatic interaction leads to the immediate and uniform formation of strong dipoles across the interface between DCS and TiO$_2$ layers,[36] which is shown in Fig. 2(e). To form a superhydrophilic TiO$_2$ surface, samples were immersed into the ethylene glycol (EG) solution of potassium hydroxide (KOH), which
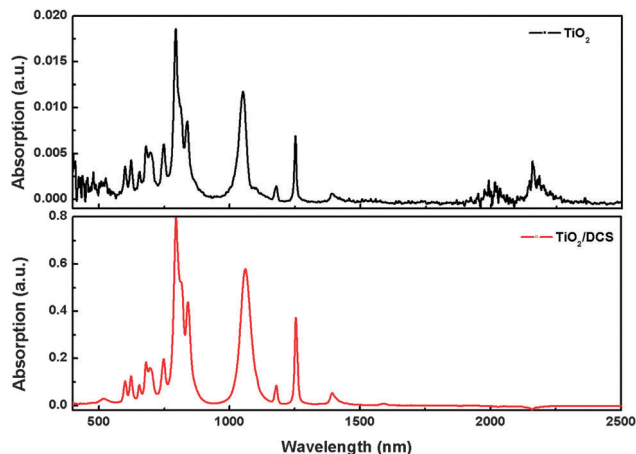
Fig. 3 Fourier Transform infrared spectroscopy (FTIR) of TiO$_2$ and DCS/TiO$_2$.

Table 1 The measured static contact angle of different materials

Material	Contact angle [°]
Bare TiO$_2$	35.12
UV treated TiO$_2$	31.94
TiO$_2$–OH	5.21
TiO$_2$/DCS	66.91

in Table 1. Generally, the high water contact angle makes it difficult to deposit a water solution on top of another layer by spin coating, but the reduced contact angle enhances the spreading of the solution, which is beneficial for the SAM occurrence of DCS. Compared to the pristine TiO$_2$ surface, an increased water contact angle of DCS (Fig. 4d) is ascribed to the surface morphology variation induced by the DCS SAM. The improved water contact angle can also enhance the film-forming property of the PCDTBT:PC$_{71}$BM solution on the TiO$_2$/DCS layer.[39]

changed surface wettability of TiO$_2$. Surface modification with SAMs can also change the wettability of the materials surface by replacing –OH terminal groups with aromatic molecular units. The changes of wettability can affect the way that the subsequently deposited organic molecules assemble and orient themselves on the surface, which can increase the density of active sites for charge transfer in the photovoltaic device.[37,38] Fourier Transform infrared spectroscopy (FTIR) was measured to prove the formation of a TiO$_2$/DCS layer. As shown in Fig. 3, the intensity of the vibronic peak of TiO$_2$/DCS is much higher than that of TiO$_2$, which supports the proposed bonding formation in the combined film. In order to investigate the hydroxylated surface of different films, surface wettability tests of the films under different conditions were performed. It can be seen from Fig. 4 that the pristine TiO$_2$ surface indicates a contact angle of 33.95° (Fig. 4a), and the superhydrophilic TiO$_2$ surface shows a low water contact angle of 5.21° (Fig. 4c), whereas an angle of 66.91° (Fig. 4d) was obtained for DCS SAM coated substrates. Meanwhile, we also irradiated the TiO$_2$ surface with UV tube, and the water contact angle of 32.76° (Fig. 4b) confirmed that UV radiation only changed the water contact angle a little. All of the data of the contact angle are listed
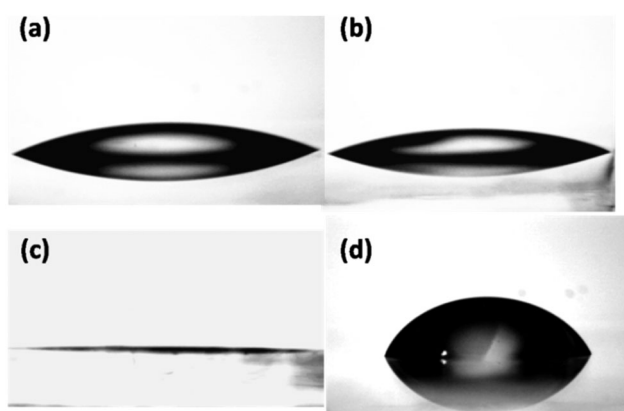
3.2 Device characteristics

Fig. 5a displays the representative current density–voltage (J–V) characteristics of control and TiO$_2$/DCS based PSCs. The control device (Device A) possessing the structure of ITO/TiO$_2$/PCDTBT:PCBM/MoO$_3$/Ag exhibited an efficiency comparable to those of previously reported devices, which had an open-circuit voltage (V_{oc}) of 0.809 V, a J_{sc} value of 13.637 mA cm^{-2}, and a FF value of 51.17%, resulting in a PCE of 5.642%. Compared to the control device, the values of J_{sc}, V_{oc}, and FF for Device C increased to 14.831 mA cm^{-2}, 0.865 V, and 54.24%, respectively, leading to a PCE of up to 6.959%. All the photovoltaic parameters of PSCs in this study are summarized in Table 2, which are the typical average of 32 devices. The dark J–V curves of inverted PSCs with and without DCS interfacial layers were measured and are demonstrated in Fig. 5b, and the optimized devices with the interfacial dipole layers showed smaller leakage current at negative voltages and low positive voltages. In addition, higher current in the space charge limited current dominated regime was achieved with DCS, suggesting an increase of charge transfer and a decrease of series resistance. The enhanced dark J–V characteristics of DCS based devices are also reflected in the increased FF (Table 2).[40,41] The incident photon-to-electron conversion efficiency (IPCE) of all fabricated devices is indicated in Fig. 5c, whose trend is consistent with Fig. 5a. Additionally, the IPCE increased ratio (ΔIPCE) of optimized devices with respect to the control device is included in Fig. 5d, and the PSCs with the TiO$_2$/DCS interfacial layer exhibit a greatly increased IPCE response in the visible region. Through integration of IPCE data of all devices, the photocurrent within the wavelength region of 450 to 650 nm significantly increased, which is in accordance with J–V characteristics of PSCs.[42–44]

It is worthy noting that V_{oc} indeed be enhanced by introducing the DCS interlayer because of the increase of built-in potential, which is strong evidence for better properties of an ideal diode.

To prove the increased contact potential difference after coating the DCS nanolayer on the TiO$_2$, the work-function measurements of TiO$_2$ and TiO$_2$/DCS layers (Fig. 6a) were carried

Fig. 4 The contact angles of the surface for (a) TiO$_2$, (b) UV-tread TiO$_2$, (c) hydroxylated TiO$_2$, and (d) DCS.

This journal is © the Owner Societies 2016
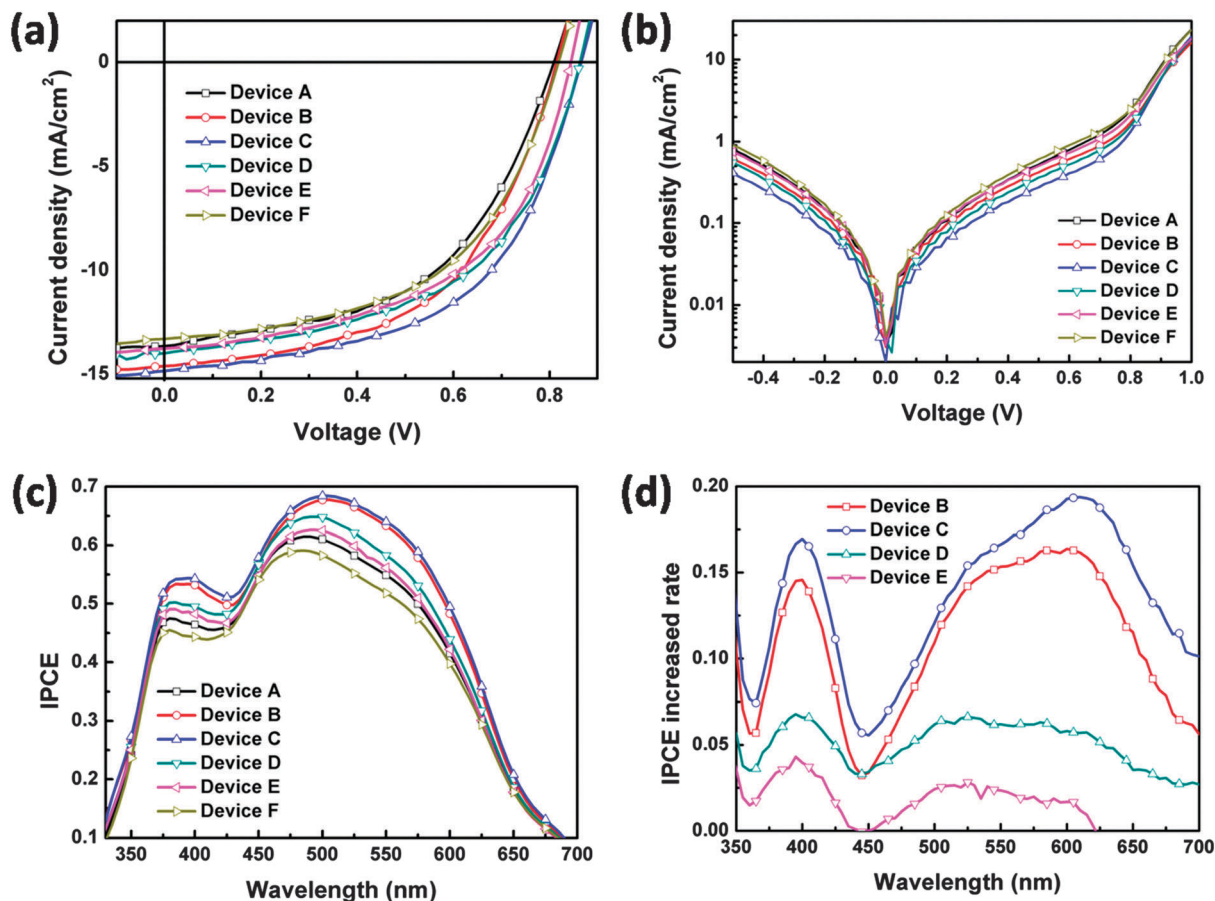
Phys. Chem. Chem. Phys., 2016, **18**, 16005–16012 | **16007**

Fig. 5 (a) J–V characteristics of devices without and with the DCS layer, (b) J–V characteristics of devices in the dark, (c) IPCE of PSCs without and with DCS layers, (d) IPCE increased rate of PSCs with DCS layers.

Table 2 The detailed performance parameters of polymer solar cells without and with different thicknesses of DCS SAM

	DCS thickness (nm)	V_{oc}	J_{sc}	FF	PCE
Device A	0	0.809	13.637	51.17	5.642
Device B	1	0.814	14.601	53.01	6.303
Device C	3	0.865	14.831	54.24	6.959
Device D	6	0.863	13.983	52.81	6.373
Device E	9	0.844	13.749	52.86	6.133
Device F	12	0.818	13.286	52.78	5.737

Fig. 6 (a) Work function of ITO, TiO_2, and TiO_2/DCS. (b) UPS of the TiO_2/DCS film.

out using a Kelvin probe system (KP 6500 Digital Kelvin probe, McAllister Technical Services Co., Ltd). The work functions of the composite TiO_2/DCS and pristine TiO_2 layers are −4.08 eV and −3.92 eV, and the addition of the DCS nanolayer can apparently realize the work function shift of TiO_2. Therefore, the enhancement of device performance is ascribed to the variation of the work function and better slope of energy alignment between TiO_2 and PCBM induced by the DCS interfacial dipole layer, which not only increased the built-in potential between the cathodes and anodes but also accelerated the extraction of charged carriers from photoactive layers, leading to the enhanced V_{oc}, FF, and J_{sc}. Ultra-violet photoelectron spectroscopy (UPS) (Fig. 6b) was used to measure the surface chemical composition and the energy level of nanocrystals of TiO_2/DCS,
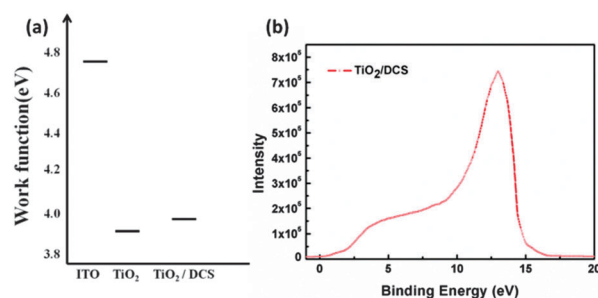
which is consistent with the result of work function measurements. However, V_{oc}, J_{sc}, and FF of Devices E and F tend to decrease, which originates from the decreased electrical conductivity.[45,46] During the formation of the TiO_2/DCS layer, the negative conjugated polymer backbone with hydrophobic properties preferentially locates at the side of the organic active layer, whereas the cationic bromide counterions are located at the hydrophilic inorganic TiO_2, and this spontaneous orientation would lead to the formation of permanent dipoles at the TiO_2/active layer interface. Fig. 7 shows how the energy level variation is affected by the spontaneously oriented dipoles on
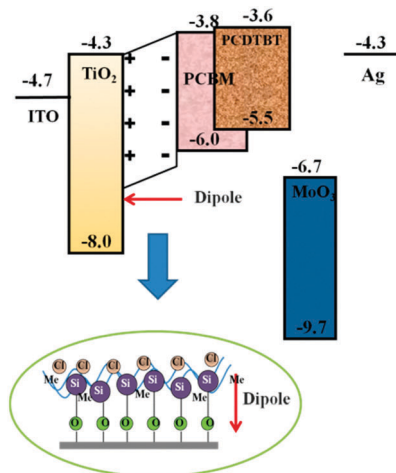
Fig. 7 The effect of the DCS SAM on the variation of the energy level structure of PSCs.

the TiO$_2$ surface, and the formation of permanent dipoles at the TiO$_2$/active layer interface leads to an electric field that is in opposite directions to the original electric field. Hence, the band edge of TiO$_2$ shifts and the energy barrier for electron injection/transport reduces after the DCS layer is deposited. Consequently, the TiO$_2$/DCS layer facilitates electron injection and transport by reducing the energy barrier between the transparent cathode and the organic active layer (Fig. 7). The work function shift can be ascribed to the lowered electrostatic potential at the surface of the TiO$_2$ layer caused by the surface dipole that is induced by the formation of an ionic double layer between the electron-accepting TiO$_2$ surface (oxygen parts) and the electron-donating DCS surface (–Cl). Due to the work function shift in Fig. 7, the operating principle can be explained after the enhanced device performance was achieved by capping the DCS nanolayer on the TiO$_2$ film. As is illustrated in the flat energy band diagram (Fig. 8), the conduction band energy level of the TiO$_2$ layer is shifted toward the lower energy level. This shifted conduction band of the TiO$_2$ layer leads to the increased built-in electric

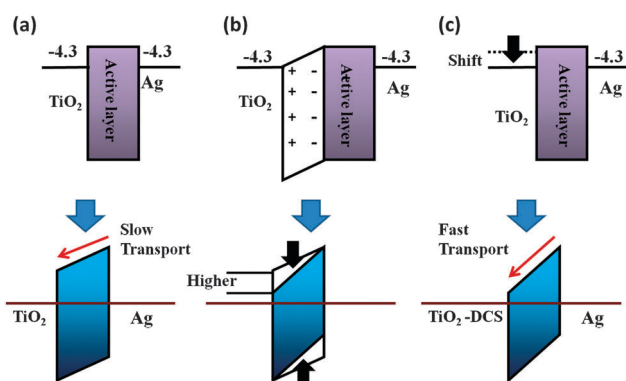Fig. 8 (a) Schematic energy diagrams and slow electron transfer for the flat band condition of TiO$_2$, (b) energy level variation affected by the spontaneously oriented dipoles on the TiO$_2$ surface, and (c) schematic energy diagrams and fast electron transfer for the flat band condition of the TiO$_2$/DCS layer.

field (or voltage), which is demonstrated in Fig. 8c, contributing to the improved V_{oc}.[47] Meanwhile, the increased V_{bi} resulted in the larger energy band bending of the active layer (PC$_{71}$BM) under short-circuit conditions and the photogenerated electrons (after charge separation) can move quickly toward the TiO$_2$ layer (Fig. 8c), which is also verified by the decreased series resistance (R_s) from 230 to 182 Ω. The fast electron transport is considered to enable the enhanced J_{sc} and FF. Thus, the DCS nanolayer on the TiO$_2$ film could increase both V_{oc} and J_{sc} at the same time, leading to an enhanced PCE.

3.3 Operation mechanism

To further explore the influence of the DCS modification layer on the device performance, the surface morphology of the interfacial layer is studied. Fig. 9 presents the atomic force microscopy (AFM) images of pristine TiO$_2$ and the TiO$_2$/DCS layers. Different thicknesses of the DCS layer (1 nm, 3 nm, and 9 nm) resulted in the relative rougher surface owning an increased root mean square roughness (RMS) of 0.293 nm (Fig. 9b), 0.304 nm (Fig. 9c), 0.415 nm (Fig. 9d) compared to 0.279 nm for the bare TiO$_2$ layer (Fig. 9a). As shown in Fig. 9e–h, the section phase image of the corresponding surface is selected to investigate interfacial adhesion, where the unique phase separation pattern of the ionomer is obtained, suggesting a complete coverage of the DCS ionomer on the TiO$_2$ surface. DCS SAMs capping layer onto TiO$_2$ leads to a significant change in the consistency of surface grains, which increases flatness of intrinsic limitations for sol–gel TiO$_2$. The enlarged RMS would provide an improved interfacial adhesion between the TiO$_2$ and active layer, and consequently facilitates charge transport at the TiO$_2$/active layer interface. The improved interfacial coherence and enhanced electrical conductivity of PSCs mentioned above reduce the energy barrier and energy loss as well.[48,49] The photocurrent of the device is thereby improved, which is responsible for the high photo-responsivity. By contrast, a 9 nm thin layer of DCS exhibits an exorbitant RMS, which results in higher surface roughness. The exorbitant roughness of the buffer layer is unexpected, which would result in a reduced bond between the electrode and the active layer.

In addition, AFM images of active layer films grown on untreated TiO$_2$ and DCS coated TiO$_2$ (the optimum device) are shown in Fig. 10. The active layer film on the DCS/TiO$_2$ forms smaller crystallites with a RMS of 0.366 with respect to that coated on the TiO$_2$ layer (0.384). Moreover, the photoactive layer deposited on the DCS surface shows an obvious and homogeneous phase separation, which was not observed from that grown on the TiO$_2$ surface. It has been well acknowledged that continuous interpenetrating networks with an appropriate domain size are essential for the efficient exciton separation and charge transport, which are important factors in the improvement of J_{sc} and FF. The better morphology of the DCS optimized devices is consistent with the higher efficiency compared to the control devices. These effects may be attributed to the better compatibility of the organic layer with the less-hydrophilic DCS-coated TiO$_2$ film rather than bare TiO$_2$ with the hydrophilic property. Even if the minor variation of the film morphology would have a negligible impact on the optical and
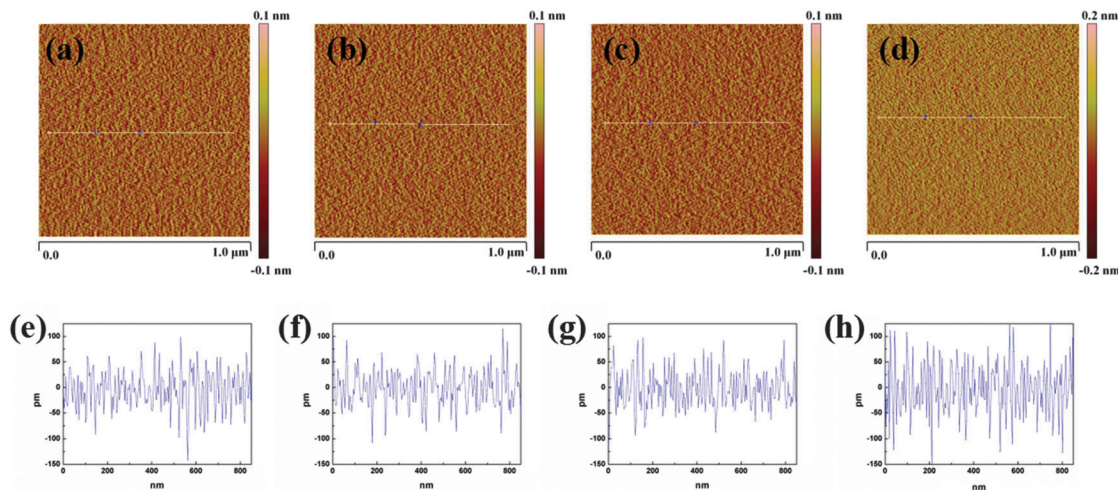
This journal is © the Owner Societies 2016

Phys. Chem. Chem. Phys., 2016, 18, 16005–16012 | 16009

Fig. 9 AFM topography image of (a) TiO$_2$ film for Device A, (b) TiO$_2$/DCS film for Device B, (c) TiO$_2$/DCS film for Device C, and (d) TiO$_2$/DCS film for Device D; section phase image of the corresponding surface of (e) TiO$_2$ film for Device A, (f) TiO$_2$/DCS film for Device B, (g) TiO$_2$/DCS film for Device C, and (h) TiO$_2$/DCS film for Device D.
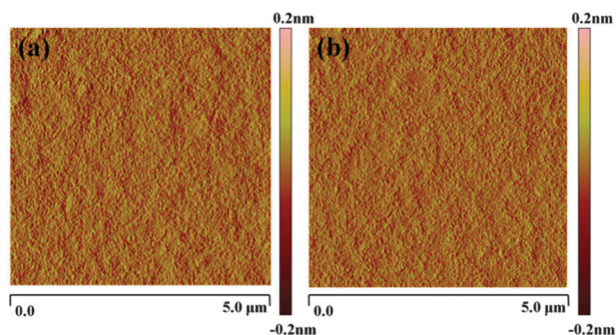

Fig. 10 AFM topography image of the active layer for (a) control device and (b) optimal device.

electrical properties of the polymer semiconductors, the changes of surface energy and wettability play an important role in the initial growth behavior of the active layer, leading to an enhanced device performance.[50,51]

To deeply understand the operation mechanism DCS, Fig. 11a reveals the dependence of the photocurrent density (J_{ph}) on the effective voltage (V_{eff}), recorded under illumination at 100 mW cm^{-2} for the control and DCS based devices. Here $J_{ph} = J_L - J_D$ and $V_{eff} = V_o - V_{app}$, where J_L and J_D are the current densities under illumination and dark, respectively, V_o is the voltage when $J_L = J_D$, and V_{app} is the applied voltage.[52,53] Apparently, J_{ph} linearly increases with the voltage at a low value of V_{eff} and then saturates at a sufficiently high value of V_{eff}. The values of the saturation photocurrent density (J_{sat}) can be determined from Fig. 11a, which is independent of the bias and temperature. Simultaneously, G_{max} can be obtained using the equation $J_{sat} = qG_{max}L$, where q is the electronic charge and L is the thickness of the active layer. The values of G_{max} for the control and DCS based devices are 8.54 × 10^{27} m^{-3} s^{-1} (J_{sat} = 13.67 mA cm^{-2}) and 9.33 × 10^{27} m^{-3} s^{-1} (J_{sat} = 14.93 mA cm^{-2}), respectively. Thus, an enhancement of G_{max} occurs after incorporating DCS into the device. Furthermore, the exciton
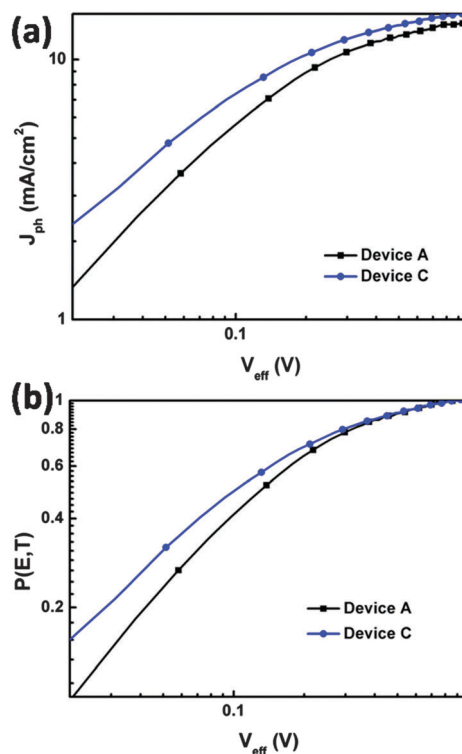

Fig. 11 (a) Photocurrent density (J_{ph}) plotted with respect to effective bias (V_{eff}) for the control (Device A) and optimal devices (Device C), and (b) exciton dissociation probability [$P(E,T)$] plotted with respect to effective bias (V_{eff}) for these PSCs.

dissociation probabilities [$P(E,T)$] were investigated, which are related to the electric field (E) and temperature (T). J_{ph} can be expressed using the equation $J_{ph} = qG_{max}P(E,T)L$.[54,55] The increased value of $P(E,T)$ indicates that the incorporation of DCS also facilitates excitons to dissociate into free carriers, and both the exciton generation rate and the dissociation probability were increased, thereby enhancing the photocurrent
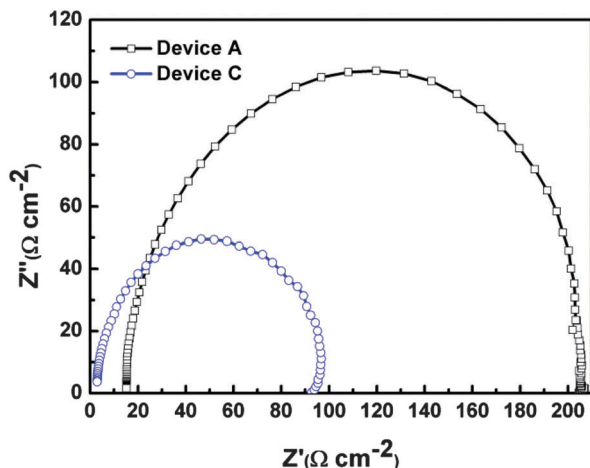
Fig. 12 Impedance spectra of Device A and Device C.

of PSCs. The charge transport and recombination dynamics of all devices were probed using electrical impedance spectroscopy. Fig. 12 presents Nyquist plots of impedance spectra for control and modified devices at open circuit applied voltage, which can help us to understand the internal resistance of different devices. The semicircle's diameter for the control devices is much larger than that of DCS based devices, which demonstrates that the recombination resistance of the modified devices is apparently decreased, suggesting that the TiO$_2$/DCS buffer layer effectively facilitates electron transfer from the active layer to ITO. Meanwhile, the series resistance of the DCS coated device is obviously reduced, which contributes to the increase of J_{sc} and FF.[56]

4. Conclusions

Small molecule DCS was employed as a self-assembled monolayer onto the TiO$_2$ electron transporting layer to improve the J_{sc}, V_{oc}, and FF of PSCs. This work principle has been ascribed to the lowered work function (conduction band energy) of the TiO$_2$ layer *via* the formation of an interfacial dipole layer at the interfaces, which was supported by the Kelvin probe measurements. The TiO$_2$/DCS cathode buffer layer ulteriorly decreased the energy barrier between the electrode and the active layer material, which was attributed to the improved physical contact between TiO$_2$ and the active layer due to the relatively improved surface coherence of the TiO$_2$/DCS layer. As a result, the overall (average) efficiency of the inverted PSCs with the DCS layers has been increased to 6.959%. This study demonstrates the capability of the DCS SAM as an efficient molecular modification layer to optimize the electrical contact between the hydrophobic organic layer and the hydrophilic metal oxide, and improved electron transfer and surface-state passivation in polymeric photovoltaic devices were achieved.

Acknowledgements

Notes and references

1 D. Yang, P. Fu, F. J. Zhang, N. Wang, J. Zhang and C. Li, *J. Mater. Chem. A*, 2014, **2**, 17281.
2 Z. C. He, C. M. Zhong, S. J. Su, M. Xu, H. B. Wu and Y. Cao, *Nat. Photonics*, 2012, **6**, 591.
3 X. G. Guo, N. J. Zhou, S. J. Lou, J. Smith, D. B. Tice, J. W. Hennek, R. P. Ortiz, J. T. L. Navarrete, S. Y. Li, J. Strzalka, L. X. Chen, R. P. H. Chang, A. Facchetti and T. J. Marks, *Nat. Photonics*, 2013, **7**, 825.
4 K. S. Lee, J. A. Lee, B. A. Mazor and S. R. Forst, *Light: Sci. Appl.*, 2015, **4**, e288.
5 E. D. Kosten, J. H. Awater, J. Parsons, A. Polman and H. A. Awater, *Light: Sci. Appl.*, 2013, **2**, e45.
6 S. J. Liu, K. Zhang, J. M. Lu, Z. Zhang, H. L. Yip, F. Huang and Y. Cao, *J. Am. Chem. Soc.*, 2013, **135**, 15326.
7 S. K. Hau, H. L. Yip, N. S. Baek, J. Zou, K. O'Malley and A. Jen, *Appl. Phys. Lett.*, 2008, **92**, 253301.
8 W. J. Zeng, H. B. Wu, C. Zhang, F. Huang, J. B. Peng, W. Yang and Y. Cao, *Adv. Mater.*, 2007, **19**, 810.
9 S. K. Hau, H. L. Yip and A. A. K. Y. Jen, *Polym. Rev.*, 2010, **50**, 474.
10 C. F. Guo, T. S. Sun, F. Gao, Q. Liu and Z. F. Ren, *Light: Sci. Appl.*, 2014, **3**, e161.
11 C. H. Hsieh, Y. J. Cheng, P. J. Li, C. H. Chen, M. Dubosc, R. M. Liang and C. S. Hsu, *J. Am. Chem. Soc.*, 2010, **132**, 4887.
12 R. Steim, S. A. Choulis, P. Schilinsky and C. J. Brabec, *Appl. Phys. Lett.*, 2008, **92**, 093303.
13 J. Y. Kim, S. H. Kim, H. H. Lee, K. Lee, W. L. Ma, X. Gong and A. J. Heeger, *Adv. Mater.*, 2006, **18**, 572.
14 Y. Sun, J. H. Seo, C. J. Takacs, J. Seifter and A. J. Heeger, *Adv. Mater.*, 2011, **23**, 1679.
15 T. Yang, K. Sun, X. Liu, W. Wei, T. Yu, X. Gong, D. Wang and Y. Cao, *J. Phys. Chem. C*, 2012, **116**, 13650.
16 C. Waldauf, M. Morana, P. Denk, P. Schilinsky, K. Coakley, S. A. Choulis and C. J. Brabec, *Appl. Phys. Lett.*, 2006, **89**, 233517.
17 G. Li, C. W. Chu, V. Shrotriya, J. Huang and Y. Yang, *Appl. Phys. Lett.*, 2006, **88**, 253503.
18 S. Lee, B. Koo, J. Shin, E. Lee, H. Park and H. Kim, *Appl. Phys. Lett.*, 2006, **88**, 162109.
19 B. C. Park, S. H. Yun, C. Y. Cho, Y. C. Kim, J. C. Shin, H. G. Jeon, Y. H. Huh, I. C. Hwang, K. Y. Baik and Y. I. Lee, *Light: Sci. Appl.*, 2014, **3**, e222.
20 B. Y. Yu, A. Tsai, S. P. Tsai, K. T. Wong, Y. Yang, C. W. Chu and J. J. Shyue, *Nanotechnology*, 2008, **19**, 255202.
21 F. Huang, K.-S. Chen, H.-L. Yip, S. K. Hau, O. Acton, Y. Zhang, J. D. Luo and A. K.-Y. Jen, *J. Am. Chem. Soc.*, 2009, **131**, 13886.
22 D. J. Lipomi, B. C. K. Tee, M. Vosgueritchian and Z. N. Bao, *Adv. Mater.*, 2011, **23**, 1771.

This journal is © the Owner Societies 2016

Phys. Chem. Chem. Phys., 2016, **18**, 16005–16012 | **16011**

23 R. Steim, S. A. Choulis, P. Schilinsky and C. Brabec, *Appl. Phys. Lett.*, 2008, **92**, 093303.

24 P. Heremans, D. Cheyns and B. P. Rand, *Acc. Chem. Res.*, 2009, **42**, 1740.

25 X. Chen, B. H. Jia, Y. A. Zhang and M. Gu, *Light: Sci. Appl.*, 2013, **2**, e92.

26 Z. C. Holman, S. D. Wolf and C. Ballif, *Light: Sci. Appl.*, 2013, **2**, e106.

27 Y. H. Su, Y. F. Ke, S. L. Cai and Q. Y. Yao, *Light: Sci. Appl.*, 2012, **1**, e14.

28 C. Yi, K. Yue, W. B. Zhang, X. Lu, J. Hou, Y. Li, L. Huang, G. R. Newkome, S. Z. Cheng and X. Gong, *ACS Appl. Mater. Interfaces*, 2004, **6**, 14189.

29 C. Yi, R. Hu, H. Ren, X. Hu, S. Wang, X. Gong and Y. J. Cao, *J. Photonics Energy*, 2014, **4**, 043099.

30 S. K. Hau, Y. J. Cheng, H. L. Yip, Y. Zhang, H. Ma and A. K. Y. Jen, *ACS Appl. Mater. Interfaces*, 2010, **2**, 1892.

31 Z. Q. Li, X. Y. Zhang, C. Y. Liu, Z. H. Zhang, J. F. Li, L. Shen, W. B. Guo and S. P. Ruan, *ACS Appl. Mater. Interfaces*, 2006, **8**, 8224.

32 C. Xie, L. Chen and Y. Chen, *J. Phys. Chem. C*, 2013, **117**, 24804.

33 S. K. Hau, H. L. Yip, H. Ma and A. K. Y. Jen, *Appl. Phys. Lett.*, 2008, **93**, 233304.

34 Z. Q. Li, X. Y. Zhang, C. Y. Liu, Z. H. Zhang, Y. Y. He, J. F. Li, L. Shen, W. B. Guo and S. P. Ruan, *J. Phys. Chem. C*, 2015, **119**, 26747.

35 R. A. Hatton, S. R. Day, M. A. Chesters and M. R. Willis, *Thin Solid Films*, 2001, **394**, 292.

36 H. Kang, S. Hong, J. Lee and K. Lee, *Adv. Mater.*, 2012, **24**, 3005.

37 R. S. Mane, W. J. Lee, H. M. Pathan and S. H. Han, *J. Phys. Chem. B*, 2005, **109**, 24254.

38 J. Min, Y. N. Luponosov, Z. G. Zhang, S. A. Ponomarenko, T. Ameri, Y. F. Li and C. J. Brabec, *Adv. Energy Mater.*, 2014, **4**, 1400816.

39 C. Peng, Y. Thio and R. Gerhardt, *J. Phys. Chem. C*, 2010, **114**, 9685.

40 X. Gong, M. Tong, F. G. Brunetti, J. Seo, Y. Sun, D. Moses, F. Wudl and A. J. Heeger, *Adv. Mater.*, 2011, **23**, 2272.

41 S. R. Cowan, A. Roy and A. Heeger, *Phys. Rev. B: Condens. Matter Mater. Phys.*, 2010, **82**, 245207.

42 A. Pivrikas, G. Juška, A. J. Mozer, M. Scharber, K. Arlauskas, N. S. Sariciftci, H. Stubb and R. Österbacka, *Phys. Rev. Lett.*, 2005, **94**, 176806.

43 O. Blum and N. T. Shaked, *Light: Sci. Appl.*, 2015, **4**, e322.

44 D. Lepage, A. Jimenez, J. Beauvais and J. J. Dubowski, *Light: Sci. Appl.*, 2012, **1**, e28.

45 G. J. Wang, T. G. Jiu, G. Tang, J. Li, P. D. Li, X. J. Song, F. S. Lu and J. F. Fang, *ACS Sustainable Chem. Eng.*, 2014, **2**, 1331.

46 J. Meyer, S. Hamwi, M. Kroger, W. Kowalshy, T. Riedl and A. Kahn, *Adv. Mater.*, 2012, **24**, 5408.

47 T. Vallant, J. Kattner, H. Brunner, U. Mayer and H. Hoffmann, *J. Phys. Chem. B*, 1998, **102**, 7190.

48 N. Sekine, C. H. Chou, W. L. Kwan and Y. Yang, *Org. Electron.*, 2009, **10**, 1473.

49 T. Yang, M. Wang, C. Duan, X. Hu, L. Huang, J. Peng, F. Huang and X. Gong, *Energy Environ. Sci.*, 2012, **5**, 8208.

50 W. Ma, C. Yang, X. Gong, K. Lee and A. J. Heeger, *Adv. Funct. Mater.*, 2005, **15**, 1617.

51 X. C. Li, F. X. Xie, S. Q. Zhang, J. H. Hou and W. C. Choy, *Light: Sci. Appl.*, 2015, **4**, e273.

52 G. Li, V. Shrotriya, J. Huang, Y. Yao, T. Moriarty, K. Emery and Y. Yang, *Nat. Mater.*, 2005, **4**, 864.

53 J. D. Chen, C. H. Cui, Y. Q. Li, L. Zhou, Q. D. Ou, C. Li, Y. F. Li and J. X. Tang, *Adv. Mater.*, 2015, **27**, 1035.

54 P. W. M. Blom, V. D. Mihailetchi, L. J. A. Koster and D. E. Markov, *Adv. Mater.*, 2007, **19**, 1551.

55 V. D. Mihailetchi, J. Wildeman and P. W. M. Blom, *Phys. Rev. Lett.*, 2005, **94**, 126602.

56 H. Choi, H. B. Kim, S. J. Ko, J. Y. Kim and A. J. Heeger, *Adv. Mater.*, 2015, **27**, 892.

16012 | *Phys. Chem. Chem. Phys.*, 2016, **18**, 16005–16012

This journal is © the Owner Societies 2016